

A direct interrogation of superfluidity on molecular scales

A. V. Benderskii,^{a)} J. Eloranta, R. Zadoyan,^{b)} and V. A. Apkarian^{c)}
Department of Chemistry, University of California, Irvine, California 92697-2025

(Received 5 February 2002; accepted 25 April 2002)

Time-resolved, pump-probe measurements are used to directly interrogate dissipative fluid dynamics in bulk He-II, on molecular scales, as a function of temperature and pressure. The Rydberg transitions of the triplet He₂^{*} excimers, which solvate in bubble states in liquid helium, are used as nanoscale transducers to initiate and to directly monitor the motion of the fluid in the form of damped oscillations of a 13 Å spherical bubble. The oscillations are damped out after one period, with a temperature-dependent period that directly tracks the normal fraction. As such, the bubble oscillator acts as a nanoviscosimeter. Through simulations of the observed signals, it is established that the coherent response of the bath obeys hydrodynamic equations of motion of a continuum subject to two-fluid flow. Dissipation occurs through two distinct channels: (a) Radiation of sound in the farfield, driven by the acceleration of volume in the compressible fluid; (b) temperature-dependent drag in the near-field. The drag can be considered to be strictly viscous in origin, or due to ballistic scattering of rotons from the bubble edge. The experiments do not distinguish between these two microscopic models. With this caveat in mind, it can be concluded that for these breathing modes of bubble states, the macroscopic concepts of superfluidity scale down to molecular dimensions. The simulations also yield effective potentials that describe the coupling between the compressible Rydberg electron and the compressible fluid. © 2002 American Institute of Physics. [DOI: 10.1063/1.1485955]

I. INTRODUCTION

One of the most direct manifestations of quantum collective dynamics on macroscopic scales is superfluidity, which occurs naturally in liquid ⁴He below its λ-point phase transition at 2.17 K.^{1,2} The unusual properties of this phase (He-II), such as its vanishing viscosity, suprathermal conductivity, and thermomechanical effect, are well explained by the phenomenological two-fluid model that was advanced by Landau,³ soon after the discovery of the effect by Kapitza.⁴ The model postulates that He-II is composed of temperature-dependent fractions of normal fluid and superfluid, the latter having zero viscosity and entropy. The first direct verification of two types of flow in He-II was provided by Andonikashvili, who used a rotating disk viscosimeter to measure the temperature dependence of the normal fraction.⁵ The model is rooted physically by associating the normal fraction with the thermally populated elementary excitations (phonons and rotons), while the superfluid fraction is associated with the ground state condensate. Otherwise, both the defining observable of inviscid flow and the successful two-fluid model, are inherently macroscopic in their nature. To what extent do these concepts remain useful on microscopic molecular scales? We address this query most directly, through experiments designed to characterize microscopic flow. This is accomplished through time-resolved pump-probe measurements in bulk He-II,⁶ using Rydberg transi-

tions of the molecular He₂^{*} centers as transducers to initiate and monitor motion of the fluid. We then consider the extent to which the observable liquid dynamics can be understood in terms of the dissipative equations of motion of two-fluid flow (viscous and potential). To carry out the experiments, we have devised optical strong-field excitation as a convenient method for preparing the triplet He₂^{*} excimers in bulk He-II.⁷ To understand the coupling between the molecular centers and the liquid, we have presented accurate calculations of the interaction between He atoms and the triplet He₂^{*} in its various Rydberg states,⁸ and detailed their solvation structure and energetics.⁹ These serve as a background. Here, we attempt to extract all system parameters from the experiment.

The quest for microscopic manifestations of superfluidity,¹⁰ and the harnessing of their consequent implications, are among the motivations of the flourishing field of molecular spectroscopy in LHe.¹¹⁻¹⁴ Key to the development of this field has been the advent of methods for injecting foreign atoms and molecules in solid, liquid,¹⁵⁻¹⁷ and cluster He.^{12,14} Of these, the cluster beam approach has been particularly fruitful. Through the pickup technique,¹⁸ the seeding of superfluid He droplets with a large variety of molecular impurities has been possible, and many special features of the LHe environment have been highlighted. The droplets are very cold and inert,¹⁹ so that delicate molecular states, such as the quartet state of Na₃, may be stabilized.^{20,21} Their high cooling capacity forecasts novel molecular engineering,²² nicely exemplified by the demonstration that HCN assembles in long linear chains, as opposed to the more stable tighter complexes that form in the absence of the

^{a)}Present address: Department of Chemistry, Columbia University, New York, New York 10027.

^{b)}Present address: Intralase, Inc., Irvine, California.

^{c)}Author to whom correspondence should be addressed; electronic mail: aapkaria@uci.edu

bath.²³ That the droplets are superfluid is very likely to play a role in these and similar observations. However, this nature is not directly elucidated by the experimental observables. Superfluidity of the heterogeneous droplet can be inferred from simulations,²⁴ on the basis of microscopic definitions such as particle–particle exchange lengths,²⁵ or quantized circulation,²⁶ which are not experimentally observable. Hence, the discovery of well-resolved rovibrational spectra,²⁷ indicative of nearly free rotation of the molecular impurity, has generated excitement as a possible microscopic reporter of superfluidity. It is in this context that the experiments on OCS doped helium clusters were presented by Toennies *et al.* as the microscopic version of the Andronikashvili experiment.²⁸ They observed that OCS undergoes nearly free rotation in droplets of ⁴He, which are superfluid; while based on the loss of spectral definition, it was concluded that the molecule does not rotate in droplets of ³He, which are normal. Moreover, in mixed ³He/⁴He clusters, a shell of ~ 60 ⁴He atoms around the molecule was sufficient for the resumption of rotation, to conclude that two solvent shells were sufficient to establish microscopic superfluidity. That the ⁴He droplet acts as an inviscid bath in response to molecular motions is to be inferred from the contrast between ⁴He and ³He clusters. Otherwise, the information content in the molecular spectra about the bath is convoluted in line shapes, a unique interpretation of which is a nontrivial challenge. Indeed, Kagan *et al.* have argued that the spectral difference in ⁴He versus ³He clusters can be understood in terms of Bose versus Fermi statistics of accessible states, rather than superfluidity.²⁹ Further, they point out that in the absence of flow proper the phenomenon may not be observable in finite size clusters. This does not contradict the fact that the spectra may be modeled through irrotational hydrodynamics,³⁰ or quantum path integral Monte Carlo simulations to extract properties such as the superfluid fraction, according to microscopic definitions.³¹ It is simply that, without further information regarding the bath, spectroscopically detected free rotation does not, in itself, imply superfluidity. To be sure, the very sharp rovibrational spectra of small impurities isolated in solid hydrogen do not imply that the solid host is fluid.³²

Notwithstanding the elegance of the cluster experiments, and the important insights that have developed from the theoretical analysis of the large spectroscopic database that has emerged, there are important reasons to resort to measurements in the bulk. Principle among these is the elimination of finite size effects inherent to clusters, all implications of which may not be fully appreciated. The size of the cluster dictates the long-wave cutoff of the phonon dispersion curve and curtails flow. The boundary limits radiative modes of dissipation and introduces surface ripples as new dissipation channels. Moreover, the preparation of He droplets through evaporative cooling limits the accessible thermodynamic state variables to a single point on the P - T plane, $T=0.38$ K ($T=0.15$ K is accessed in mixed ³He/⁴He clusters). This leaves open the issue of the onset of microscopic superfluid behavior, and precludes direct connections with the characteristic temperature and pressure dependence of the macroscopic phenomenon. To our knowledge, our ex-

periments are the first of their kind. They are conducted in the bulk, as a function of temperature and pressure. We monitor dynamics of the fluid as it modulates the electronic energy spacings of a molecular chromophore, as opposed to monitoring internal motions of a molecular probe. We follow motion of the fluid through time domain measurements, which is essential to follow dissipative dynamics in condensed media.

Due to the self-purifying nature of LHe, molecular spectroscopy in bulk He is limited to studies of the intrinsic electronic excitations, to atomic, He*, and molecular, He₂* , Rydberg states.³³ Based on analysis of line shapes, and the observation of rotational structure in selected He₂* transitions, it had been established that as in the case of excess electrons,^{34,35} both atomic^{36,37} and molecular^{38,39} Rydberg states form solvation bubbles around them. In essence, the strong Pauli exchange repulsion between outer electron and He forces the liquid to recede, to form a microcavity around the excited center. Moreover, it had been established that the excimers undergo nearly free rotation, with rotational relaxation times of 1 ms.⁴⁰ While this would not be surprising for angularly isotropic bubble states, rotation also occurs in strongly anisotropic states.⁹ These findings have been revisited and confirmed in more recent studies.^{41,42} Notably, all of the known spectral observables of the molecular centers evolve continuously across the phase transition, without a signature for the role of the superfluid phase. The same holds for Rydberg transitions of atomic impurities, which exhibit broad spectral profiles.^{43–45} Dephasing limits the information content of frequency domain spectra to the instantaneous forces between chromophore and bath, without providing clues about modes and mechanisms of dissipation, which are essential to characterize the nature of the bath. To obtain information about the system at times beyond the electronic coherence window, it is necessary to resort to time–domain methods, and, in particular, to pump–probe measurements, as amply demonstrated in other condensed phase systems.⁴⁶

Our experimental paradigm is straightforward. We rely on the triplet He₂*-bubble states to measure the liquid response attendant to the sudden promotion of a Rydberg electron. The potential energy curves of the relevant states, as a function of bubble radius, are collected in Fig. 1. These curves are based on *ab initio* pair potentials, and density functional methods for describing the fluid.⁹ The metastable He₂* $a^3\Sigma_u^+(2s)$, which occurs in a spherical bubble of 6.9 Å radius, serves as our initial state. Although this is the lowest-energy electronically excited state in LHe, at 18 eV above ground, it lies in the windowless XUV. Nevertheless, by taking advantage of the intense electric fields generated in ultrashort laser pulses, the excimers can be prepared optically, through controlled strong-field ionization and recombination processes.⁷ Under repetitive strong-field irradiation, a steady-state concentration of He₂(a) is sustained. A short laser pulse is then used to promote the $2S$ electron from the ³ a state, ~ 10 ms after preparation of the excimer, after complete thermalization. Vertical excitation from the equilibrium geometry of the bubble will necessarily lead to a repulsive interaction with the liquid (see Fig. 1). The bubble must expand to accommodate the excited electron, and must undergo

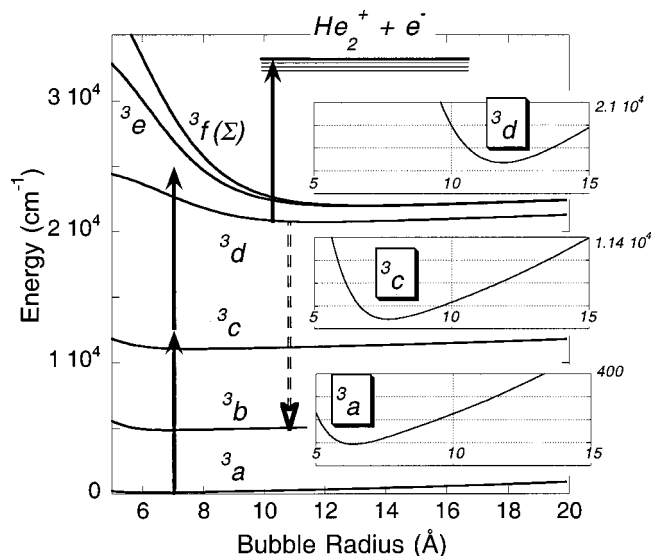


FIG. 1. Potential energy curves of the He_2^* triplet Rydberg states in liquid He, as a function of the bubble radius. The magnifications of the relevant states are shown as insets, with a 400 cm^{-1} range of the ordinate. The curves are based on *ab initio* pair potentials, and density functional methods for treating the liquid, as described in Ref. 9. The pump-probe measurements in the fluorescence depletion mode is illustrated by the arrows. The pump prepares the 3d state via the two-photon resonance, and the $^3d \rightarrow ^3b$ emission serves as signal. As the bubble expands, the laser becomes resonant with the ionization limit. Ionization prevents the bubble from reaching the 3d state minimum to emit, the probe acts by depleting the fluorescence.

damped oscillations until reaching equilibrium on the excited state. A time-delayed copy of the pulse is used to probe the effect of the excitation, relying on the $^3d \rightarrow ^3b$ fluorescence as a signal. To the extent that the energy gap between the various Rydberg states depends on the bubble radius, the electronic resonances will be modulated as the bubble oscillates. It is the damping of the oscillations of the bubble that we seek, since this would describe dissipation in the fluid. As we show, a unique interpretation of the underlying dynamics can be extracted from the experimental signals, using two-fluid hydrodynamics, and without the benefit of any auxiliary input. In the companion paper, we carry out time-dependent density functional simulations of the same system, using *ab initio* input parameters.⁴⁷

In what follows, in Sec. II, we describe the experimental details; and in Sec. III we collect the main experimental observations. A detailed analysis of the observations is given in Sec. IV, as we develop the inescapable conclusions serially. A discussion of the most significant results is revisited in the Conclusions in Sec. V.

II. EXPERIMENT

The experiments are conducted in an Oxford liquid helium cryostat equipped with five sets of optical windows, yielding a base temperature of 1.45 K under saturated vapor pressure. Temperature is controlled to $\pm 0.05 \text{ K}$ with a wire heater, and by throttling the helium pump. Experiments were conducted in the temperature range from 1.45 K to the λ point, where advantage is taken of the extremely high thermal conductivity of He-II. This ensures that the excitation volume returns to complete thermal equilibrium in less than

10^{-7} s .⁴⁸ A reproducible generation of the excimers below the threshold for laser breakdown can only be accomplished below the superfluid transition temperature. To measure the effect of applied external pressure on the dynamics, a LHe pressure cell equipped with four sapphire windows was designed to fit inside the cold shaft of the cryostat. He gas was fed into the cell through a 1/4 in. tube, allowed to liquify at the base temperature of 1.6 K and maintained under controllable pressure in the range from 0 to 5 atm.

The time-resolved pump-probe measurements to be reported are single colored. We use the output of a regeneratively amplified Ti-Sapphire laser ($\lambda = 790 \text{ nm}$, $\text{FWHM} \approx 20 \text{ nm}$), with a pulse width of $\sim 80 \text{ fs}$. The majority of the conducted experiments are two-pulse measurements, in which the laser beam is split into two nearly equal intensity pump and probe arms. An optical delay of up to 4 ns is introduced in one arm, using a retroreflector cube mounted on a 1.2 m translation stage. The pump and probe beams are then recombined colinearly using a beamsplitter, and are focused through the same lens to maximize their overlap in the liquid. The signal consists of the induced fluorescence over the $\text{He}_2^*(^3d \rightarrow ^3b)$ transition at 640 nm, which is collected perpendicular to the excitation axis using a two lens relay, dispersed through a 1/4 m monochromator, and detected with a photomultiplier.

A detailed analysis of the steps that lead to the strong-field preparation of the Rydberg states of He_2^* have already been given.⁷ As a first step, controlled ionization of the liquid helium is achieved by a subcritical cascade of electrons that are ponderomotively accelerated by the laser field (80 fs, 790 nm, 10^{13} W/cm^2) to kinetic energies above the ionization potential of the ground state He atom (24.6 eV). Subsequent fast dimerization $\text{He}^+ + \text{He} \rightarrow \text{He}_2^+$ and recombination of the ions, $\text{He}_2^+ + e^- \rightarrow \text{He}_2^*$, forms the neutral excimers in concentrations of the order of 10^{13} cm^{-3} . The excimer formation kinetics has a fast component of the order of 100 ps, followed by a slower rise on the time scale of several ns. At a 500 Hz laser repetition rate, all excitations decay during the 2 ms interval between pulses with the exception of $\text{He}_2^*(^3a)$, which is the lowest electronically excited state in LHe. This long-lived triplet excimer, whose radiative decay is strongly spin forbidden, serves as a trap of the excited population. A steady-state $\text{He}_2^*(^3a)$ concentration of 10^{12} cm^{-1} accumulates, as described in Ref. 7, sufficient to be used for the time-resolved measurements. The 100 ps component of the formation of $\text{He}_2^*(^3a)$ by the pump pulse, is observed by the probe pulse through two-photon-induced fluorescence over the $^3d \rightarrow ^3b$ transition as a rising background (Fig. 2). This component can be easily separated from the pump-probe signal of $\text{He}_2^*(^3a)$ generated by the previous pulse, by subtracting traces obtained at a laser repetition rate of 500 Hz from those obtained at 100 Hz. Since the concentration of excimers that survive over $t = 2 - 10 \text{ ms}$ from the previous pulse is controlled by diffusion-limited triplet-triplet annihilation $C(t) \approx 1/Kt$, their concentration is 5 times smaller at 100 Hz, therefore their contribution to the signal is 5 times weaker. In contrast, the contribution to the signal from excimers freshly generated by the pump pulse is independent of repetition rate. Here we are interested in the time-resolved

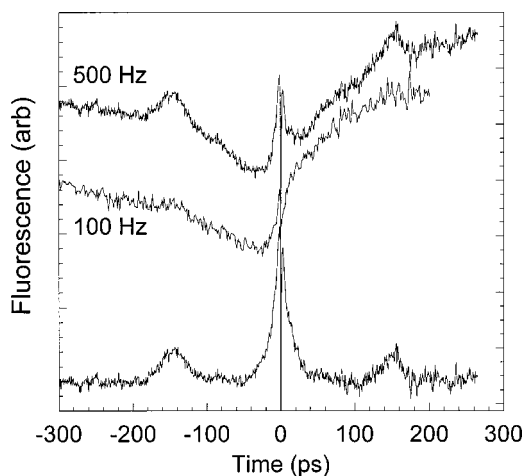


FIG. 2. Pump-probe signals recorded at a laser repetition rate of (a) 500 Hz, (b) 100 Hz, and (c) the difference between (a) and (b).

dynamics of the laser excited excimers after their preparation, as such, the signals of interest are those obtained after the subtraction shown in Fig. 2. The time inversion asymmetry of the signal in Fig. 2 is due to the unequal intensities in the pump and probe beams. An example of the signal obtained with equal intensity beams, with careful alignment to eliminate beam walkoff by the long delay line, is shown in Fig. 3 along with a magnification of the region around $t = 0$. The required inversion symmetry in such scans enables the assessment of features due to noise. The sharp dip in the signal at $t = 0$ seen in the inset of Fig. 3, is strictly an electronic coherence artifact, an interference between pump and probe beams sensitive to the angle between the two beams.

In another set of experiments, a three-beam arrangement was used. The first, high-power beam generates the excimers, and the two weak beams serving as pump and probe arrive ~ 10 ns later (a fixed optical delay) to interrogate the dynamics of the excimers generated by the first beam. The delay between the weak pump and probe beams is varied using a computer-controlled translation stage. The obtained signals, now without the rising background, were identical to

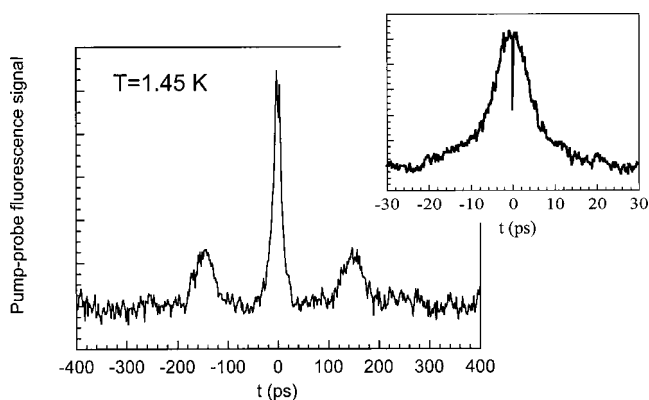


FIG. 3. The signal obtained with balanced intensities in pump and probe arms is symmetric with respect to time inversion (a contrast with Fig. 2). The inset shows a magnification of the $t = 0$ region (the negative spike at $t = 0$ is due to interference between the collinear pump and probe beams—a coherence artifact).

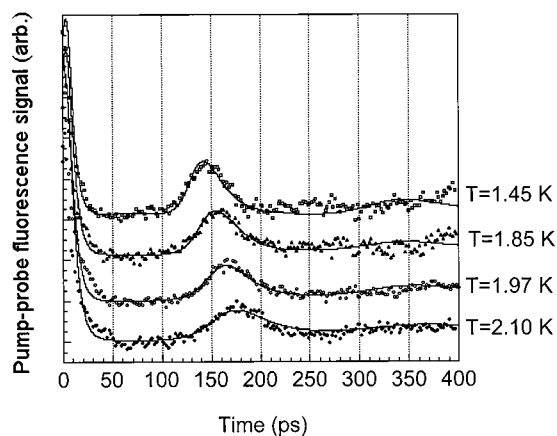


FIG. 4. Pump-probe-induced fluorescence over the ${}^3d \rightarrow {}^3b$ transition, recorded at different temperatures. Solid lines are the result of simulations of the two-fluid hydrodynamic equations of motion (16), including compressibility.

those obtained with the two-beam setup after the subtraction scheme. However, the signal-to-noise ratio in this arrangement was significantly poorer than that obtained in the two-beam setup. The three-beam experiments are sensitive to the noise arising from the pulse-to-pulse variation in the concentration of excimers generated by the pump pulse. In the two-beam experiment, the number of excimers interrogated 2 ms after production is determined mostly by the bimolecular annihilation kinetics, $C \propto 1/Kt$, which is essentially independent of the initial concentration produced by the previous laser pulse. Thus, the bimolecular triplet-triplet annihilation kinetics provides a “noise filter” in these measurements.

III. RESULTS

Examples of the pump-probe signal at different temperatures are shown in Fig. 4. The signal starts at $t = 0$ as a maximum. It then decays on the time scale of 4 ps, and reappears at $\tau = 140\text{--}200$ ps, albeit with reduced amplitude and broadened to a FWHM of ~ 30 ps. The $t = 0$ signal arises from the solvent configuration fixed by the initial 3a state, therefore from a bubble of radius $R = 6.9$ Å. The decay of the signal occurs during evolution of the solvent on the excited state, therefore, during the expansion of the bubble. The recursion in the signal must, accordingly, be associated with the recompression of the bubble to reach its initial configuration. The time of this recursion, τ , yields the breathing period of the bubble. Only one recursion is observable, indicating that the bubble oscillation is fully damped after one period of motion. More precisely, since the signal-to-noise ratio at the first recursion is ~ 5 , if there is a second recursion, its amplitude must be a factor of 5 weaker.

As the temperature is raised, the recursion time increases and its amplitude is reduced (see Fig. 4). We discover that the temperature dependence of the breathing period tracks that of the normal fraction, $\rho_n(T)/\rho$, as illustrated in Fig. 5. In the temperature range of the experiment, to a good approximation, the normal fraction can be given as a power law: $\rho_n(T)/\rho = (T/T_\lambda)^{5.72}$.⁴⁹ Similarly, the data can be empirically fit to the form

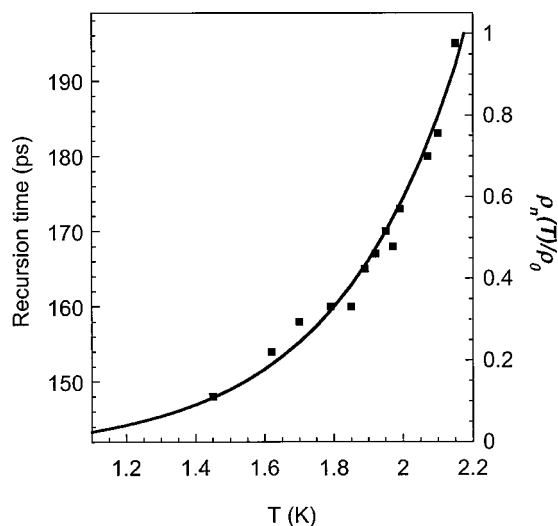


FIG. 5. Temperature dependence of the breathing period of the bubble tracks the normal fraction. The filled squares are the experimental recursion times (left axis) of the bubble, the solid line is the normal fraction (right axis) of He-II. The plot is nearly identical to that obtained by Andonikashvili using a macroscopic disk viscosimeter (Ref. 5).

$$\frac{1}{\tau} = \frac{1}{\tau_0} - \frac{1}{\tau_\lambda} \left(\frac{T}{T_\lambda} \right)^n, \quad (1)$$

with $\tau_0 \equiv \tau(T \rightarrow 0) = 146 \pm 2.3$ ps, $\tau_\lambda \equiv \tau(T = T_\lambda) = 575 \pm 32$ ps, and $n = 5.9 \pm 0.9$.

Measurements were carried out as a function of pressure, starting from the saturated vapor pressure (0.569 Torr at 1.6 K),¹ up to three atmospheres. The observed signals are shown in Fig. 6. The breathing period of the bubble shows a linear dependence on pressure, as illustrated in Fig. 7. As the pressure is increased, the signal weakens without changing its overall shape. The pressure-induced quenching of the 3d state fluorescence is well documented previously,⁵⁰ and we have suggested that this may arise from penetration of the liquid into the nodal region of the Rydberg $3S$ electron in

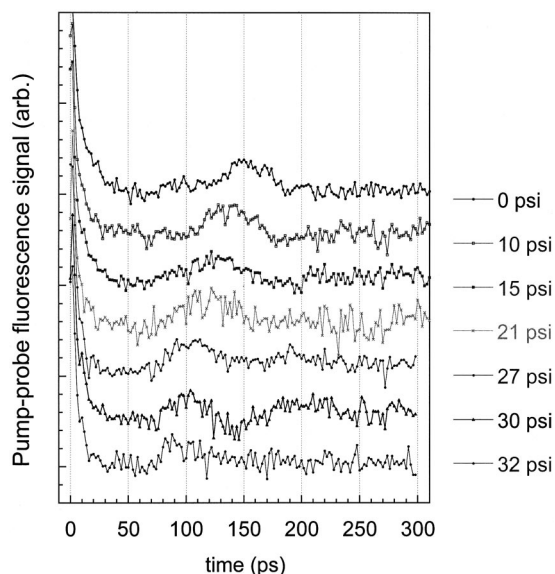


FIG. 6. The pump-probe signal as a function of pressure.

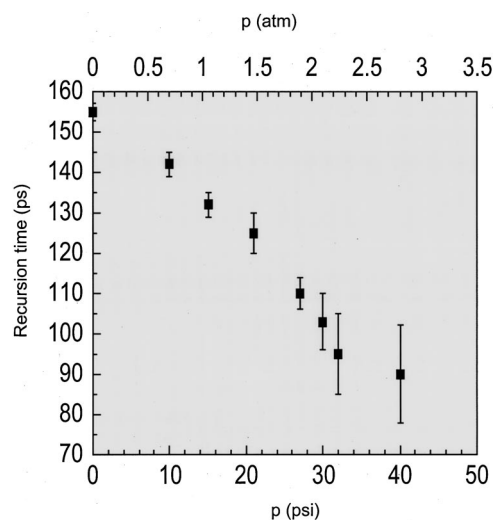


FIG. 7. The dependence of the bubble breathing period on pressure.

this state.⁹ The fact that the shape of the signal is not affected by pressure would imply that the relevant pump and probe windows remain unchanged along the nuclear coordinates.

Measurements were carried out at the saturated vapor pressure, as a function of the relative polarization between pump and probe lasers. When normalized, signals obtained with parallel and perpendicular polarization are indistinguishable. Their absolute magnitudes are comparable. These single color experiments were also carried out as a function of color. Using a slit in the oscillator compressor, the Ti:Sapphire laser pulses were stretched to 200 fs, and tuned from 780 to 810 nm. Within this tuning range, the signal profiles are insensitive to color. Measurements were also carried out as a function of the intensity of one beam, while the other is kept fixed (e.g. the data of Fig. 3 versus Fig. 4), to establish that the monitored $^3d \rightarrow ^3b$ fluorescence is two-photon induced.⁷

IV. ANALYSIS AND DISCUSSION

A. The pump-probe resonances

Given the stack of Rydberg states that are accessible with short intense pulses from the 3a state, and the fact that we are carrying out single color experiments at relatively high intensities, the assignment of the pump and probe windows that yield the observable signal is not immediately obvious. Consultation of the potential energy curves of the relevant Rydberg states shown in Fig. 1 is instructive. The laser is nearly resonant with the $^3c(v=1) \leftarrow ^3a$ and $^3d(v=2) \leftarrow ^3c(v=1)$ transitions. Therefore the observed $^3d \rightarrow ^3b$ emission as a function of delay between the pump and probe could be expected to yield the time evolution of a wave packet on the 3c state. Indeed, this was the intent of the original design. However, given the high intensity of the pulses, 10^{13} W/cm², and the very large transition dipoles involved, $\mu_{ca} = 5.4$ D and $\mu_{dc} = 4.5$ D, it becomes clear that the single-photon resonances are fully saturated. For example, in a 100 fs pulse, the $^3c \leftarrow ^3a$ transition will undergo ~ 100 Rabi cycles ($n = \mu E \Delta t / \hbar$) within the pulse duration. Under the pulse, a coherent superposition of Rydberg states, composed

of all states that are dipole connected with significant detunings from one-photon resonances (all electronic states shown in Fig. 1) will be prepared. While the population transferred to 3c is a sensitive function of the time-intensity product of the laser, the population transferred to the 3d state can be shown to be fairly robust.⁴⁷ Under a large range of intensities, the population becomes nearly exclusively divided between the 3a and 3d states, which are separated by a two-photon resonance at 780 nm. This is consistent with the observation that the 3d fluorescence has quadratic dependence on the laser intensity. Due to the large volume of the 3e , 3f , and higher Rydberg electrons, the states above 3d are dramatically blue shifted when the liquid is held at its equilibrium structure on the 3a state. However, upon expansion of the bubble past 10 Å on the 3d state, the laser becomes resonant with the ionization limit (see Fig. 1). The observed pump-probe signal can therefore be expected to arise from fluorescence depletion. At $t=0$, the 3d state is prepared, and observed through its prompt fluorescence over the $^3d \rightarrow ^3b$ transition. As the bubble expands, the probe laser ionizes the 3d state, depleting the observable fluorescence. This presumes that the thermalized electron-hole pairs recombine predominantly on the lowest triplet surface, namely the 3a state, as had previously been inferred.⁷ As the bubble recompresses, the ionization limit is dramatically shifted up in energy, the resonance is lost, and the fluorescence resumes.

It is easily established that the internal coordinates of the excimer do not participate in the observed recursions. The vibrational period of the excimer is ~ 20 fs ($\omega_e = 1500 \text{ cm}^{-1}$),⁵¹ significantly shorter than the width of the laser pulse. As such, the laser prepares the excimer in its vibrational eigenstate. The absence of polarization dependence rules out contributions of molecular rotation to the signal, which in any case would evolve on the time scale of < 2 ps ($B = 7 \text{ cm}^{-1}$).⁵¹

These considerations provide the rationale for the observable signal, and give state assignments that will turn out to be consistent with the observed dynamics. Nevertheless, except for the mechanism of observing bubble dynamics by the present experimental approach, in what follows we will not have recourse to the specifics of the above arguments. Instead, we will extract all pertinent information regarding energetics and dynamics through the analysis of the experimental signals.

B. Hydrodynamic mass, size, and shape of the bubble

Let us focus on the most prominent feature of the signal, the observed recursion that occurs on the time scale of 150–200 ps, which was already identified as the breathing period of the bubble on the electronically excited state. The observed period betrays a large oscillator mass, which can be reconciled with that of a ~ 10 Å bubble if hydrodynamics were assumed to hold on this length scale.⁵² Thus, assuming harmonic motion, $\tau = 2\pi(\mu/K)^{1/2}$, taking the restoring force constant for radial motion to be that of surface tension, γ , using the macroscopic value of $\gamma = 0.18 \text{ cm}^{-1}/\text{Å}^2$, therefore $K = 8\pi\gamma$; an effective mass $\mu \sim 750 m_{\text{He}}$ is obtained for $\tau = 150$ ps. According to Rayleigh, the hydrodynamic mass of

the spherical breathing mode of a bubble in an ideal liquid is three times that of the displaced liquid, $\mu = 4\pi R^3 \rho$.⁵³ Using the density of the liquid, $\rho = 0.1448 \text{ g cm}^{-3}$, the deduced mass leads to the estimate $R_e = 13$ Å for the equilibrium radius of the bubble on the excited state. This coincides with the calculated equilibrium radius of the bubble in the 3d state (see Fig. 1). Independent of that, the estimate would seem reasonable in view of the known equilibrium radius of an excess electron in LHe of 17.2 Å,⁵⁴ and the expectation that the Rydberg electron must be more compact due to the presence of the He_2^+ ion core. With the same token, it is possible to establish that the observed motion is that of a monopole (spherically symmetric breathing mode), rather than quadrupole or higher poles that would be excited if Rydberg states other than $l=0$ were accessed. For harmonic multipolar distortions of a bubble internal to an ideal liquid, subject to the restoring force of surface tension, the period of motion is given as⁵⁵

$$\tau = 2\pi \left(\frac{\rho R^3}{\gamma n(n-1)(n+2)} \right)^{1/2}, \quad (2)$$

with $n=2$ representing the quadrupolar mode.⁵⁶ A period of 150 ps would now imply a bubble radius of 26 Å, which is unacceptable, since this is significantly larger than the radius of the bare electron in LHe.

We may conclude the following:

(a) The observed period identifies the motion as that of the monopolar breathing of a bubble of ~ 13 Å radius, consistent with what would be expected for a liquid He cavity formed around an excited $l=0$ Rydberg state (the 3d state).

(b) The period is consistent with the hydrodynamic mass of the bubble and the macroscopic value of surface tension, which suggests that the fluid can be considered as a continuum on the length scale of the boundary motion of the bubble.

(c) The observation of a recursion in the signal implies coherence in nuclear coordinates, despite the strong dissipation that can be inferred from the reduced amplitude upon recursion, i.e., the bath response consisting of the equivalent of $\mu/m_{\text{He}} \sim 750$ helium atoms distributed in the liquid, maintains vibrational coherence.

To understand the essential features of the observed dissipative dynamics, our task is greatly simplified, in that the problem is reduced to the one-dimensional breathing of a sphere in the liquid. In much of the development to follow we will be concerned with the one dimensional problem of the time evolution of the bubble radius, $R(t)$.

C. Adiabaticity of the observable motion

Although a redundancy in terminology, since bubble motion corresponds to the adiabatic component of a hydrodynamic disturbance,⁵⁷ it is useful to establish that the velocities involved in the observable displacement of the liquid fall in this limit. Pump-probe signals, $S(t)$, obtained with pulses that are not phase locked, can be understood in terms of the time-dependent overlap of the evolving density, $\rho(R;t)$, with stationary resonance windows, $W(R)$: $S(t) \propto \int W(R)\rho(R,t)dR$. The initial decay of the signal occurs

with a half-life of ~ 5 ps. This fluorescence depletion must occur as the bubble radius expands out of the initial thermal distribution of radii projected by the pump window. Thus, a resonance window width of $\Delta R \sim 1 \text{ \AA}$, given by the thermal amplitude of the bubble radius R in the 3a state, can be assumed. Accordingly, we may estimate that in its fastest phase of motion, the bubble expands at a velocity of $\dot{R} \sim 20 \text{ m s}^{-1}$. Since this velocity is below the Landau critical velocity of $v_c = 60 \text{ m/s}$, the motion of the bubble cannot create elementary excitations in the liquid.⁵⁸ Since the velocity of the fluid must decay (quadratically) as a function of distance from the bubble edge, we recognize that velocity of the fluid everywhere is small in comparison to the speed of sound, $v(r)/c \ll 1$ ($c = 230 \text{ m/s}$). This is the criterion for adiabaticity of motion, which in turn implies that⁵⁹ (a) the normal and superfluid densities, ρ_n and ρ_s of He-II, are separately conserved; (b) dissipation will be governed by terms linear in velocity; (c) in the near-field, for $r < \lambda_c$, where λ_c is the wavelength of sound, the fluid can be treated as incompressible. This, in turn, implies that in the near-field (viscous) drag is the only source of dissipation.

Based on the estimated hydrodynamic mass, $\mu \sim 750 m_{\text{He}}$, the requirement of adiabaticity of motion, $\dot{R} < 60 \text{ m s}^{-1}$, can only be met for kinetic energies below $\sim 400 \text{ cm}^{-1}$. The repulsive wall accessed vertically from the initial 3a state dictates the energy imparted to the bubble. If this is in significant excess beyond the adiabatic limit, then dissipation through shock waves is to be expected. Shocks do not constitute a direct observable in the fluorescence depletion measurements, since they do not modulate the electronic resonances of the chromophore during the probe period. Although we are solely concerned with the experimentally observable dynamics of the bubble, we recognize that this may be preceded by the generation of shock waves.⁶⁰

D. Dissipation due to two-fluid drag in the near-field

The most direct evidence that the microscopic bubble dynamics reports on the superfluidity of the bath, is the observation that the breathing period of the bubble is directly proportional to the normal fraction, as illustrated by the data of Fig. 5. Such a behavior would be expected if the motion were damped by the drag experienced from the normal fraction. To see this, recall that for a harmonic oscillator damped by friction, $\ddot{Q} + (4\pi/\tau_\eta)\dot{Q} + (2\pi/\tau)Q = 0$, the observed period, τ' , is related to the natural period, τ , and the damping time constant, τ_η , through

$$1/\tau' = [(1/\tau)^2 - (1/\tau_\eta)^2]^{1/2}. \quad (3)$$

Although the breathing motion of the bubble is far from harmonic, it would nevertheless be expected that the period will stretch as a function of increasing drag, as τ_η approaches the natural period τ . The connection between the drag experienced by the microscopic bubble and the macroscopic viscosity of the fluid is central to our inquiry. As such, we develop it with some care.

In the linearized dissipative equations of motion of two-fluid hydrodynamics,⁵⁹ which is validated by the adiabaticity condition, the superfraction behaves as an ideal fluid:

$$\rho_s \frac{d\mathbf{v}_s}{dt} + \nabla P_s = 0, \quad (4)$$

while the normal fraction obeys the Navier–Stokes equation:

$$\rho_n \frac{d\mathbf{v}_n}{dt} + \nabla P_n = \left(\frac{4\eta}{3} + \zeta \right) \nabla(\nabla \cdot \mathbf{v}_n) - \eta \nabla \times \nabla \times \mathbf{v}_n, \quad (5)$$

where η and ζ represent the shear and second viscosities of the normal fluid. Since we are interested in the irrotational motion of a monopole, $\nabla \times \mathbf{v} = 0$; and since the $v(r)/c \ll 1$, we may assume the liquid to be incompressible in the near-field, $\nabla \cdot \mathbf{v} = 0$. Then, the right side of (5) drops, and the motion of the fluid is prescribed through the velocity potential, $\mathbf{v} = \mathbf{v}_s = \mathbf{v}_n = \nabla \phi(r, t)$. With this substitution, we may sum (4) and (5) to obtain

$$\rho \left(\frac{\partial \nabla \phi}{\partial t} + \frac{1}{2} \nabla v^2 \right) = -\nabla P_n - \nabla P_s, \quad (6)$$

where $\rho = \rho_n + \rho_s$ has been used. For an incompressible fluid, the velocity potential consistent with the spherical boundary conditions, $v(r=R) = \dot{R}$ and $v(r=\infty) = 0$, is⁵⁵

$$\phi(r) = -R^2 \dot{R}/r. \quad (7)$$

Substituting this in (6), and after integrating over the volume between the limits of bubble edge and infinity, we obtain

$$\rho \left(R\ddot{R} + \frac{3}{2} \dot{R}^2 \right) = P_n(r=R) + P_s(r=R) - P_{\text{ext}}, \quad (8)$$

where we have identified $P(r=\infty) = P_{\text{ext}}$ and have recognized that at $r=\infty$ the pressure is the sum of partial pressures of normal and supercomponents. At the boundary layer, the internal pressure of the inviscid fraction is simply given by the force potential, $U(R)$:

$$P_s(r=R) = \frac{\rho_s}{\rho} P(R) = \frac{\rho_s}{\rho} \left(\frac{-\partial U(R)/\partial R}{4\pi R^2} \right). \quad (9)$$

For the normal fraction, *only if it is assumed to be a continuum on the length scale of relevance*, the radial component of the stress is the sum of the internal pressure on the fluid and its reactive pressure due to internal friction $P = -\sigma_{rr} = P_{\text{int}} - 2\eta(\partial v/\partial r)$.⁶¹ This, at the boundary layer, reduces to

$$P_n(r=R) = \frac{\rho_n}{\rho} P(R) = \frac{\rho_n}{\rho} \left(P_{\text{int}}(R) - 2\eta \frac{\partial v}{\partial r} \Big|_{r=R} \right) = \frac{\rho_n}{\rho} \left(\frac{-\partial U(R)/\partial R}{4\pi R^2} - 4\eta \frac{\dot{R}}{R} \right). \quad (10)$$

Combining (9) and (10), we obtain the two-fluid equation of motion (EOM) for the breathing of the bubble:

$$\rho \left(R\ddot{R} + \frac{3}{2} \dot{R}^2 \right) = \frac{-\partial U(R)/\partial R}{4\pi R^2} - P_{\text{ext}} - 4\eta \frac{\rho_n}{\rho} \frac{\dot{R}}{R}. \quad (11)$$

It is valuable to note that the dissipative term in this EOM arises from the viscous drag on the boundary layer. Otherwise, the spherical symmetry of the motion ensures the absence of shearing in the bulk.

The hydrodynamic EOM (11) should be valid for a macroscopic bubble or, to the extent that both normal and superfractions act as continua. It is necessary to establish the validity of this assumption for the normal fraction. In the microscopic picture, the normal fraction consists of the excited state density for which the wave function is orthogonal to the ground state condensate. Let us focus on the rotons, since they determine the viscosity of He-II in the temperature range of the experiment.² We expect the continuum assumption to be valid, when the de Broglie wavelength associated with the thermal drift of rotons exceeds their mean separation, i.e., $\lambda_r N_r^{-1/3} \geq 1$, where N_r is the number density of rotons; and $\lambda_r = h v_r / kT \approx h v_c / kT = 28 \text{ \AA} / \text{K}$. Using the Landau–Khalatnikov expression for N_r ,⁶² it can be determined that $\lambda_r N_r^{-1/3} \sim 1$ near $T = 1.5 \text{ K}$. Thus, based on this criterion, rotons (and therefore the normal fraction) may be regarded to be a continuum for $T > 1.5 \text{ K}$, i.e., in the experimental range. In essence, the wave density of excitations is sufficiently delocalized to collectively react to changes in the boundary, with the moving boundary defined by the breathing of the bubble.

If we regard the normal fraction as the thermal population of quasiparticles, the validity of the continuum assumption becomes questionable. In this case, for the notion of a viscous response to be valid, the scattering length between quasiparticles must be small in comparison to the length scale of relevance, which is established by the breathing amplitude. The roton–roton scattering length, l_r , varies between 4.3 and 25 \AA over the range $T = 2.15$ and 1.5 K.² Thus, at the lower-temperature limit l_r becomes comparable to the diameter of the bubble of 20–30 \AA . In this limit, a gas kinetic treatment of drag would seem more appropriate. The sought quantity is the incremental pressure of rotons at the boundary layer, due to motion of the boundary. For a number density N_r of thermally populated rotons, assuming point particles, the incremental collision rate between bubble and rotons is $4\pi R^2 \dot{R} N_r$. Taking for the momentum transfer in these elastic collisions $\Delta p_r = -2\bar{p}_r$, the sought reactive pressure can be obtained as

$$P' = \frac{1}{4\pi R^2} 4\pi R^2 \dot{R} N_r 2\bar{p}_r = 2\rho_r \bar{v}_r \dot{R} = 4 \frac{\eta_r}{l_r} \dot{R}, \quad (12)$$

in which, consistent with the assumption of point-particle rotons, we have used the ideal gas relation $\eta_r = \frac{1}{2} \rho \bar{v} l_r$. To be more exact, the interaction pseudopotential between quasiparticles must be included to obtain the interparticle scattering cross sections. In the Khalatnikov–Landau treatment of quasiparticles, $\eta_r = (\pi/10) \rho_r \bar{v}_r l_r$ is found to be insensitive to the details of assumed potentials, since the roton–roton scattering occurs from the repulsive roton core of $\delta = 1\text{--}2 \text{ \AA}$.⁶³ Similarly, considerations for the microscopics of roton–bubble scattering would suggest a correction to (12). However, it is difficult to establish this correction.⁶⁴ We will instead note the gas kinetic viscosity by a prime, η' , and search for experimental guidance as to the magnitude of such a correction.

Despite the different concepts employed in arguing for the drag experienced by the microscopic bubble to be ballistic or viscous in origin, the dynamical implications are diffi-

cult to distinguish experimentally. To make a direct comparison between the predictions of the two models, substitute $1/l_r = (1/l_\lambda) \sqrt{T_\lambda/T} \rho_r / \rho$ in (12), and after equating the normal density with that of rotons, obtain the EOM in the ballistic drag limit:

$$\rho \left(R\ddot{R} + \frac{3}{2} \dot{R}^2 \right) = \frac{-\partial U(R)/\partial R}{4\pi R^2} - P_{\text{ext}} - 4\eta' \frac{\rho_n}{\rho} \left(\frac{T_\lambda}{T} \right)^{1/2} \frac{\dot{R}}{l_\lambda}. \quad (13)$$

This result should be compared with (11) for the case of viscous drag. In both cases, dissipation is strictly due to the last term. Since in the range $T = 1.45\text{--}2.17 \text{ K}$, the viscosity of the normal fraction $\eta = 1.15 \times 10^{-5} \text{ P}$ is nearly a constant,² we may obtain the temperature-dependent damping times, τ_η , predicted by the two limiting cases:

$$\tau_\eta(T) = \frac{4\pi\rho\bar{R}}{\partial P/\partial \dot{R}} = \tau_\lambda \left(\frac{T_\lambda}{T} \right)^n = \begin{cases} \frac{\pi\rho\bar{R}^2}{\eta} \left(\frac{T_\lambda}{T} \right)^{5.72}, & \text{for viscous drag;} \\ \frac{\pi\rho\bar{R}l_\lambda}{\eta'} \left(\frac{T_\lambda}{T} \right)^{5.22}, & \text{for ballistic drag,} \end{cases} \quad (14)$$

in which the overbars indicate cycle averaging.

The experimentally determined power law for the temperature dependence of the observed period is $n = 5.9 \pm 0.9$, which within its error bars is the same as what is predicted for the damping times in either model (14). However, in contrast with the harmonic case (3), a linear relation $1/\tau' = 1/\tau_0 - 1/\tau_\eta(T)$ is suggested by the experiment. To understand this empirical finding, it will be necessary to take the full anharmonicity of the motion into account, now explicitly including the interaction potential $U(R)$ in the treatment, and taking account of compressibility in the farfield. This we carry out through numerical simulations below. Accepting the empirical finding, if the damping constant $\tau_\lambda \equiv \tau(T = T_\lambda) = 575 \pm 32 \text{ ps}$ obtained from the experimental fit to (1) is interpreted in the viscous model, $\bar{R} = 14.5 \pm 1$ would be obtained. This is consistent with the estimated equilibrium radius of the bubble of 13 \AA , since due to the R^3 dependence of the hydrodynamic mass, the cycle-averaged radius must be larger than its equilibrium value. If the experimental value of τ_λ were interpreted in the ballistic limit, and $\eta' = \eta$ were assumed, then the unacceptable value of $\bar{R} = 34 \pm 2$ would be obtained. A correction factor, $\eta' \sim 0.3\eta$, would render the predictions of the two models indistinguishable.

Quite clearly, a quantitative analysis of the entire pump–probe transient, rather than just the recursion period, would be valuable. Nevertheless, we should recognize that experimentally, it will not be possible to distinguish between the two microscopic models of drag.

E. Dissipation through radiation of sound in the farfield

While the drag on the bubble drops by an order of magnitude as the temperature is dropped from 2.15 to 1.45 K, and its effect on the period can be seen to level off, the motion remains strongly damped. This can be inferred from the reduced amplitude of the recursion at 1.45 K and the absence of a second recursion. The remaining channel of dissipation must arise from the compressibility of the liquid, which was hitherto ignored. Since $v(r,t) \ll c$, the near-field contribution to dissipation via this channel must necessarily be small in comparison to that of viscosity. However, in a compressible liquid, an accelerating volume dissipates power radiatively, by generating sound in the farfield.⁶¹ The effect can be estimated from the power dissipated by a harmonic monopole:

$$\Pi = \frac{\rho}{4\pi c} \overline{\dot{V}^2} \approx \frac{\rho}{4\pi c} \left\langle 8\pi R \dot{R}^2 + \frac{4\pi R^2 \ddot{R}}{\tau} \right\rangle^2, \quad (15)$$

where the angle bracket contains the cycle-averaged acceleration of volume. Using the observed period, the estimated front velocity and bubble radius, a dissipation rate of 10^2 cm^{-1} per period is obtained, i.e., radiation of sound alone is sufficient to damp the adiabatic motion of the bubble within one or two periods. Since sound emission is contingent only upon compressibility, it is in effect temperature independent, and should persist even at $T=0 \text{ K}$, where the superfluid fraction reaches unity. The outward radiation of sound results from its finite velocity, which introduces a phase lag between edge of the bubble and displacement of the liquid in the farfield. The effect is taken into account using the retarded velocity potential, $\phi(r,t) = r^{-1} f[t - (r - R)/c]$, which for the conditions $R \ll \lambda_c$ and $r \gg R$ can be well approximated by $\phi(r,t) = R^2 \dot{R}(t - R/c)/r$. With this substitution in (6), and noting that the constant density front moves at the retarded time $t' = t - r/c$, the Herring equation of motion for a bubble in a compressible liquid is derived.^{65,66} Note that in the near-field the retarded potential reduces to the incompressible limit (11), making it clear that the drag on the boundary layer remains as before. The Herring equation, now including the two-fluid drag in the hydrodynamic limit, becomes

$$\begin{aligned} & \left(1 - 2\frac{\dot{R}}{c}\right) R \ddot{R} + \left(1 - \frac{4}{3}\frac{\dot{R}}{c}\right) \frac{3}{2} \dot{R}^2 \\ &= \frac{1}{\rho} \left[-P + \frac{\dot{R}}{c} \left(1 - \frac{\dot{R}}{c}\right) R \frac{\partial P}{\partial R} - 4\eta \frac{\rho_n}{\rho} \frac{\dot{R}}{R} \right], \end{aligned} \quad (16a)$$

where

$$P = \frac{\partial U / \partial R}{4\pi R^2}. \quad (16b)$$

In the ballistic limit the last term in (16a) must be replaced by the dissipative term developed in (13). This constitutes the final form of the EOM used in the analysis of the experimental transients. The same equation for the case of a vis-

cous single fluid (setting $\rho_n/\rho = 1$ in the last term) has been implemented in the analysis of nonpolar solvation in classical liquids.⁶⁷

F. Numerical simulations

The unknown in (16) is the effective force potential, $U(R)$, which describes the coupling between the excimer and the liquid in the excited state. We expand the effective force potential as a polynomial about the minimum, R_e . A fourth-order polynomial,

$$U(R) = \sum_{i=1}^4 c_i (R - R_e)^i, \quad (17a)$$

with parameters (energy and length in cm^{-1} and \AA units)

$$c_1 = 0, \quad c_2 = 1.3, \quad c_3 = -0.45, \quad c_4 = 0.125, \quad R_e = 13. \quad (17b)$$

To reproduce the observed signal, we use the now standard approach for treating pump-probe data.⁴⁶ An ensemble of N trajectories is propagated according to the hydrodynamic EOM (16), and inverted assuming a detection window. In the fluorescence depletion picture, the signal must disappear as the bubble stretches out of its initial equilibrium value on the 3a state. A sufficiently flexible window function that describes the effect is:

$$W(R) = \left(\frac{1 - \tanh(R - R^*)}{2} \right)^\alpha. \quad (18)$$

We use $R^* = 10.5 \text{ \AA}$ and $\alpha = 0.75$ as the location and turnover range of the window. The initial conditions of the trajectories are specified by the thermal distribution of bubble radii on the 3a state, which is represented as a Gaussian spatial distribution centered at $R = 7 \text{ \AA}$. The simulated signals are overlaid with the data in Fig. 4. The reproduction of the experimental signal profiles and their temperature dependence are nearly perfect. The same potential leads to an equally satisfactory fit to the data using the ballistic drag (13) by setting $\eta' = 0.25\eta$.

Given the good agreement between experiment and simulation, let us explore the dissipative two-fluid dynamics that governs the motion of the bubble. The essence can be understood by inspecting the three trajectories shown in Fig. 8, along with their associated energy loss plots and portraits of velocity versus radius, given in Figs. 9 and 10. In the absence of dissipation, the motion is anharmonic due to the R^3 dependence of the hydrodynamic mass. At $T = 1.45 \text{ K}$, dissipation is entirely governed by the radiation of sound, the rate of which is proportional to acceleration (of volume). Accordingly, the energy loss occurs predominantly along the repulsive wall, where the potential gradient is largest and volume acceleration is greatest. Sound cannot be emitted at constant flow, therefore, the radiative energy loss is minimal along the flat part of the potential. Radiation elongates the period of motion from its natural value of 90–145 ps, and damps it out in two periods. At $T = 2.15 \text{ K}$, drag due to the normal fraction has a significant incremental contribution to dissipation, elongating the period to 200 ps, and damping it in 1 period. Since this contribution is proportional to veloc-

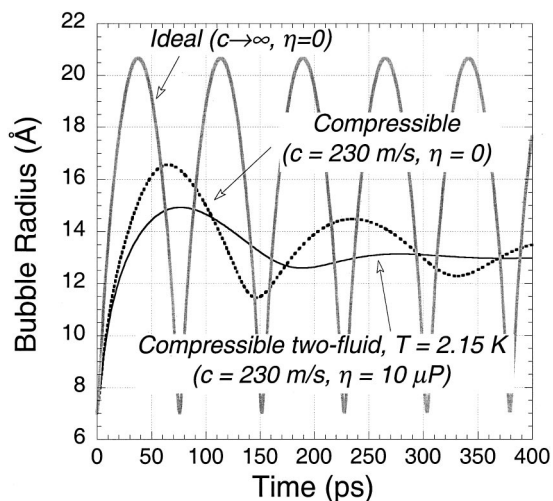


FIG. 8. Bubble trajectories calculated by numerical integration of Eq. (16), for the limiting conditions of adiabatic breathing in a liquid: (a) Nondissipative ideal liquid, $c \rightarrow \infty$, $\eta = 0$ (or $T = 0$ K). (b) Compressible superfluid, $c = 230$ m/s, $\eta = 0$ (or $T = 0$ K), in which dissipation is due to the radiation of sound alone. (c) Compressible viscous liquid, $c = 230$ m/s, $\eta = 10 \mu\text{P}$ ($T = 2.15$ K), which corresponds to that of He-II near the λ point.

ity, it dominates where the velocity would have reached its highest value, namely, on the flat portion of the potential. Radiation prevents the bubble from reaching the critical Landau velocity of 60 m/s, which is reached in the absence of dissipation.

Albeit convoluted with the window function, the pump-probe transients check important segments of this dynamics. The initial decay in the experimental signal tracks motion of the packet on the repulsive wall, as it enters the probe window. The recursion measures the spread of the initial packet and its velocity as it exits the window, after dissipation over a full cycle of motion. The drag in the near-field leads to the temperature dependent dissipation, which appears as period elongation. The quartic potential, with its positive anharmonicity, is necessary to reproduce the linear dependence of the period on normal fraction.

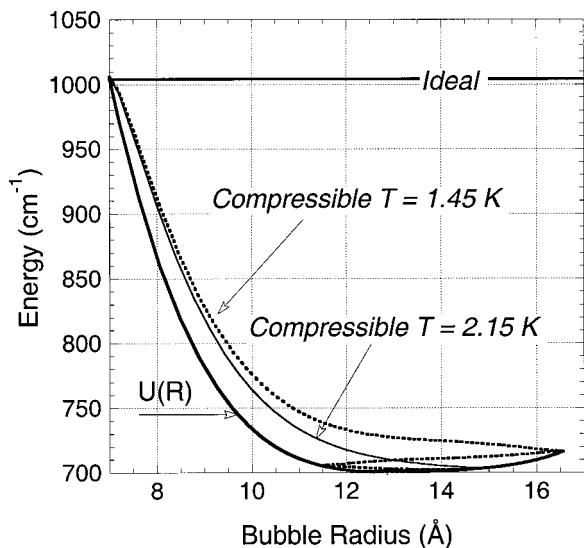


FIG. 9. Energy loss plots associated with the trajectories of Fig. 8.

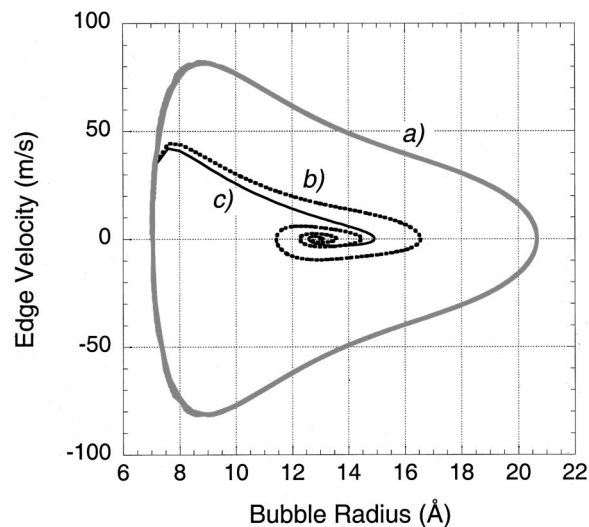


FIG. 10. Velocity portraits associated with the trajectories of Fig. 8.

All parameters of the fourth-order expansion in (17) are well determined by the requirements of reproducing the transients and their temperature dependence. Two of the simulation parameters are independently checked: the potential minimum at 13 \AA and the initial value of the trajectory at 7 \AA , are in very good agreement with the calculated bubble radii on the 3d and 3a states, respectively.⁹ It remains to consider the information content in the extracted potential. The pressure dependence studies are informative in this respect.

G. Pressure dependence and the experimentally determined effective interaction potential

The effect of external pressure would be to add the volume work, $PV = P(4\pi/3)R^3$ term to the potential in (17a). To reproduce the observed linear dependence of the breathing period on pressure, it is additionally necessary to include a pressure-dependent correction of the linear coefficient in (17b). By taking $c_1 = -12P + 1.33P^2$ (with P in atm, and c_1 in $\text{cm}^{-1}\text{\AA}^{-1}$), the experimental recursion times are reproduced to within their error bars. Representative potential curves are illustrated in Fig. 11, along with the implied shift in their minima shown in the inset. Pressure has a global effect. Besides the obvious cubic contribution to the attractive branch, the linear correction implies simultaneous stiffening of the repulsive wall. The net effect on the equilibrium radius of the bubble is insignificant up to 1 atm, but the radius shrinks from 13 to 12.2 \AA between 1 and 3 atm. These results can be qualitatively understood by considering the origin of the potential.

The potential, $U(R)$, defines the nondissipative force $\partial U/\partial R$ acting on the bubble surface, due to the many-body $\text{He}_2^* - \text{He}$ and $\text{He} - \text{He}$ interactions. Motions that are significantly faster must adiabatically follow the breathing of the bubble. This includes breathing of the Rydberg electron density $\rho_{\text{el}}(r'; R)$; and the strongly correlated bath defined through its spatial density profile, $\rho_{\text{He}}(r; R)$. Note that the

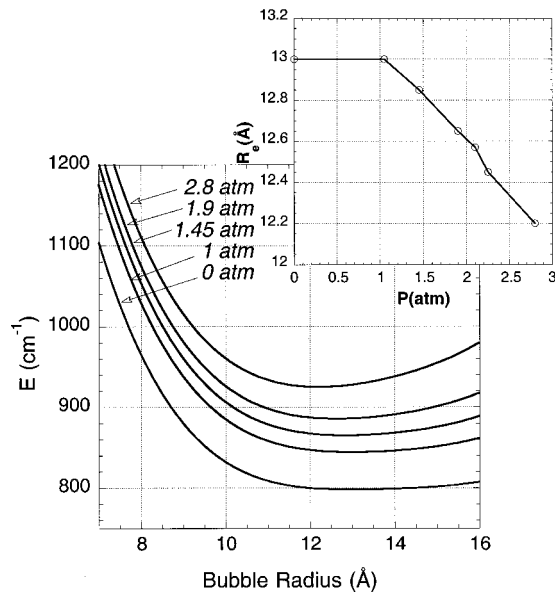


FIG. 11. Effective bubble potentials extracted from the dynamics, at different pressures. The potential minimum, which defines the equilibrium radius of the bubble, is plotted as a function of pressure in the inset. The energy offset in the plots is arbitrary.

interfacial region will have significant thickness, of several Å ,⁹ and the bubble radius used so far must be associated with the barycenter of the liquid interface:

$$\int_0^R \rho(r) d^3r = \int_R^\infty [\rho_0 - \rho(r)] d^3r. \quad (19)$$

In its simplified form, the cavity formation energy in the liquid can be expressed as

$$U(R) = \int V(|r-r'|) \rho_{\text{el}}(r';R) \rho_{\text{He}}(r;R) d^3r' d^3r + \frac{1}{8m_{\text{He}}} \int \frac{[\nabla \rho_{\text{He}}(r;R)]^2}{\rho_{\text{He}}(r,R)} d^3r - \gamma S(R) - P_{\text{ext}} V(R). \quad (20)$$

Here, $V(|r-r'|)$ may be identified as the electron–helium pseudopotential; the last two attractive terms are the work expended against interfacial tension and volume; and the second term is the quantum kinetic energy due to the gradient of the interface (quantum pressure).⁶⁸ Given the external pressure, the contribution of PV work to the potential is straightforward provided that we recognize that this will also lead to an increase of the liquid density everywhere. A detailed analysis of the microscopic surface tension shows that for small changes in R , it is possible to approximate $\gamma S = 4\pi\gamma'R^2$ with $\gamma' = 0.72\gamma_\infty$, where γ_∞ is the macroscopic coefficient of tension for a flat surface ($\gamma_\infty = 0.18 \text{ cm}^{-1} \text{ Å}^{-2}$).⁹ The remaining first two terms in (20) are strongly correlated. The kinetic term must oscillate as the bubble breadths: it increases due to thinning of the interface as the bubble compresses against the electron, and decreases as the interface thickens when the bubble expands. The Rydberg electron, especially for diffuse states, is also compressible; therefore its density is modulated by the oscillations of

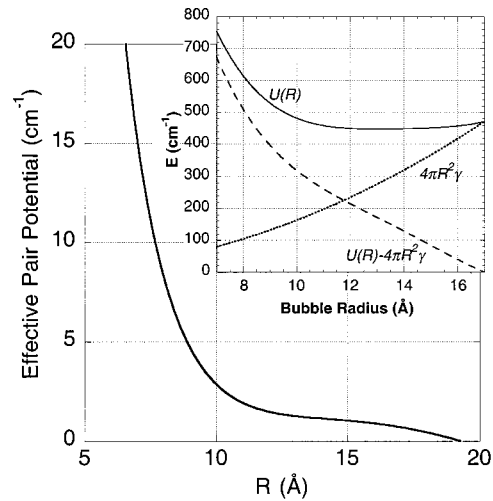


FIG. 12. The effective interaction potential between the excimer and the liquid. In the inset, the decomposition of $U(R)$, by subtracting the effect of surface tension and pressure, is shown to highlight the repulsive wall dominated by the electron–helium interaction. Deconvolution of the He density, assumed to be a Heaviside function, yields the effective pair interaction potential between the excimer and He atoms.

the bubble. The repulsion between electron and liquid results from the double convolution of the electron and liquid density profiles, as expressed by the first term in (20). We can therefore understand the pressure dependence of the extracted equilibrium radius. At low pressure, $P < 1$ atm, the interfacial kinetic energy increases by steepening of the interface about its barycenter, with little change in the bubble radius. As the pressure is increased above 1 atm, the barycenter moves in, now by compressing the electron. This strong coupling between electronic and nuclear coordinates implies nonadditivity of pair interactions, as already recognized.⁸

An approximate decomposition of the experimentally obtained effective potential is possible. The contribution dominated by the electron–helium interaction may be obtained by subtracting the PV and $\gamma'S$ contributions from the experimental $U(R)$. This is shown in the inset to Fig. 12. Assuming a heaviside function for the liquid density profile, therefore including the quantum pressure in the surface tension term in (20), the effective He_2^*-He potential, can be extracted:

$$\tilde{V}_{\text{He}_2^*-\text{He}}(R) = \frac{1}{4\pi R^2 \rho_0} \frac{\partial}{\partial R} \left(U(R) - 4\pi R^2 \gamma - P_{\text{ext}} \frac{4\pi}{3} R^3 \right). \quad (21)$$

This is shown in Fig. 12, for the meaningful range visited by the trajectories, $R = 7-17 \text{ Å}$. The effective pair potential has a long tail of a few cm^{-1} between 10–20 Å , with a characteristic shelf-type structure. This is qualitatively to be expected for the 3d state of He_2^* , since in this state the bubble is retained by the extranodal electron density of the $3S$ Rydberg electron.⁹ In contrast with the frequency domain spectra of Rydberg transitions, the time-dependent measurements are significantly more informative about the details of this

delicate interaction. Given the weak and diffuse nature of the interaction, reliable quantitative *ab initio* analyses of the coupling between a compressible electron and liquid are difficult to obtain. The extracted effective potential, which averages out the interfacial motion, should be quite useful in connecting the present analysis to treatments that rigorously take the interfacial dynamics into account.⁴⁷

V. CONCLUSIONS

Through time-resolved measurements of the coherent, damped oscillations of a 13 Å bubble in He-II, we establish that for these breathing modes, the fluid can be described as a continuum that obeys two-fluid hydrodynamics down to the scale of the boundary motion of ~ 10 Å. The temperature-dependent breathing period of the bubble tracks the normal fraction, just as in the case of the damped oscillations of the macroscopic disk viscosimeter used by Andonikashvili.⁵ To the extent that the normal fraction carries the viscosity of the fluid, the bubble serves as a nanoviscosimeter, and directly yields the T -dependent vanishing viscosity of the fluid, now on microscopic scales. A significant finding of this study is that bulk viscosity can be successfully applied to flow on the nanometer length scale.

Whether the drag experienced by the bubble in the near-field can be associated with viscosity proper, or arises from the ballistic scattering of rotons from the bubble boundary, is a meaningful microscopic distinction. In the first case, we may conclude that the macroscopic two-fluid model identically scales down to molecular lengths. The experimental data can be fit under the assumption of viscous response, using the macroscopic viscosity of the fluid, without any further adjustment. The data can also be fit using the ballistic drag model, by using the scattering cross section of rotons from the bubble boundary as an adjustable parameter. Although the power law for the temperature dependence of damping is different [see Eq. (14)], the data does not have the required accuracy to resolve this difference. As such, the experiment leaves room for speculation. The ballistic model would be expected if excitations are considered as quasiparticles, characterized by their interparticle scattering length. However, this notion must break down on molecular scales, where the spatial extent of the excitations cannot be ignored. We have argued that if we were to take the de Broglie size of rotons into account, then in the range of the study $T > 1.5$ K, the normal fraction constitutes a continuum. In the wave-dynamic picture, more appropriate in the microscopic limit, the excitation continuum would imply that the wave function orthogonal to the superfluid senses the boundary, and therefore will react to any changes in it. The collective reaction of the excited state density would imply a viscous drag, albeit due to the wave excitations of the quantum fluid. Indeed, an understanding of the scattering of rotons from molecular centers would be quite valuable in developing a complete description of molecular dynamics in a superfluid bath.

In addition to drag in the near-field, a major channel of dissipation in the breathing motion of the bubble is the radiation of sound, due to the acceleration of volume in the compressible fluid. Since this process depends on compress-

ibility alone, it is nearly independent of temperature and will remain active even at 0 K. This contribution to dissipation can be reduced by considering volume-conserving shape distortions, such as would be accessible through $\Delta l = 1$ Rydberg transitions that conserve principle quantum number $\Delta n = 0$. More generally, the radiation of sound can be expected as an important channel of dissipation in all extended media, solids and liquids, but not in small clusters.

Despite the strong dissipation, the liquid response remains coherent on time scales of 200 ps (and length scales of the order of wavelength of sound). This unusual behavior for a liquid must be associated with the quantum nature of the bath and its Bose statistics. The latter establishes the continuity scale in terms of the long-range off-diagonal density overlap,⁶⁹ which leads to the phononlike behavior of liquid ⁴He up to the length scale of internuclear distances. Thus, the response to molecular scale perturbation will be extended to the length scale of the wavelength of sound. As long as the fluid represents a continuum subject to a single velocity of first sound, its collective adiabatic dynamics may be reduced to that of a single-particle density through the Madelung transform.⁷⁰ Clearly, a single-particle density may not decohere. These are implicit assumptions in treating the fluid through classical continuum mechanics,⁶⁸ as opposed to multiparticle molecular dynamics, which would be necessary to describe a Fermi liquid.

The direct interrogation of the nature of the fluid on microscopic scales is afforded by the relatively simple coupling between the spherical molecular probe ($l = 0$) and the bath. The interaction between a Rydberg electron and He is essentially repulsive. As such, the probe presents a simple boundary to the liquid, and to a good approximation, it is the motion of the liquid as a result of the sudden change of the boundary that is observed rather than the probe. The effective potential that describes the coupling between the liquid and the excimer, was extracted from the dynamics. Wrapped in this effective potential are the motions that adiabatically follow the breathing of the bubble. These consist of the breathing of the liquid interface and the electron density. Their effect is recognized in the pressure dependence of the effective potential. The obtained potential minimum of 13 Å and the shelllike structure of the deconvoluted pair interaction, are consistent with those expected in the ³*d* state of He₂^{*}.⁸ In this state, the extranodal electron density of the 3*S* electron retains the bubble wall.⁹ The delicate coupling between this diffuse electron density and the compressible liquid interface is highlighted by the effective He₂^{*}-He pair potential shown in Fig. 12. These data should be quite useful in developing a deeper understanding of the coupled motion of electron, liquid, and interface.

Finally, let us highlight the fact that we have reported the first time domain measurements of microscopic dynamics in superfluid helium. Time domain measurements are uniquely suited for characterizing dissipative dynamics in condensed media. In contrast with frequency domain molecular spectroscopy in superfluid helium, it is the time domain nature of measurements that has allowed the characterization of dissipation in the liquid, and therefore a direct interrogation of the superfluid nature of the bath.

ACKNOWLEDGMENTS

This research was made possible through a grant from the U.S. AFOSR (F49620-01-1-0449), and a Fellowship to J.E. from the Finnish Academy. We have benefited from fruitful discussions with Professor N. Schwentner of the Free University of Berlin and with Professor P. Taborek and K. C. Janda of UCI.

- ¹J. Wilks and D. S. Betts, *An Introduction to Liquid Helium* (Oxford University Press, New York, 1987).
- ²I. M. Khalatnikov, "Phenomenological theory of superfluid ^4He ," in *The Physics of Liquid and Solid Helium*, Part I, p. 1, edited by K. H. Bennemann and J. B. Ketterson (Wiley-Interscience, New York, 1976).
- ³L. D. Landau, *J. Phys. (Moscow)* **5**, 185 (1941); **11**, 91 (1947).
- ⁴P. L. Kapitza, *Nature (London)* **141**, 74 (1938).
- ⁵E. Andonikashvili, *J. Phys. (Moscow)* **10**, 201 (1946).
- ⁶Complete reports of the experimental results and their analysis have been presented at conferences, as succinctly noted in proceedings: A. V. Benderskii, R. Zadoyan, N. Schwentner, and V. A. Apkarian, *Proc. SPIE* **3273**, 297 (1998); V. A. Apkarian, A. Benderskii, and J. Eloranta, *Am. Chem. Soc.* **220**, 136 (2000).
- ⁷A. V. Benderskii, R. Zadoyan, N. Schwentner, and V. A. Apkarian, *J. Chem. Phys.* **110**, 1542 (1999).
- ⁸J. Eloranta and V. A. Apkarian, *J. Chem. Phys.* **115**, 752 (2001).
- ⁹J. Eloranta, N. Schwentner, and V. A. Apkarian, *J. Chem. Phys.* **116**, 4039 (2002).
- ¹⁰J. P. Toennies, in *Advances in Quantum Many-Body Physics*, edited by E. Krotscheck and J. Navarro (World Scientific, Singapore, 2002), Vol. 4.
- ¹¹B. Tabbert, H. Günther, and G. zu Putlitz, *J. Low Temp. Phys.* **103**, 653 (1997).
- ¹²J. P. Toennies and A. F. Vilesov, *Annu. Rev. Phys. Chem.* **49**, 1 (1998).
- ¹³K. B. Whaley, in *Advances in Molecular Vibrations and Collision Dynamics*, edited by J. Bowman (JAI Press, Greenwich, CT, 1998), Vol. 3.
- ¹⁴J. P. Higgins, J. Reho, F. Stienkemeier, W. E. Ernst, K. K. Lehmann, and G. Scoles, in *Atomic and Molecular Beams*, edited by R. Campange (Springer-Verlag, Berlin, 2001).
- ¹⁵T. Kinoshita, K. Fukuda, and T. Yabuzaki, *Phys. Rev. B* **54**, 6600 (1996).
- ¹⁶S. Kanorsky, A. Weis, M. Arndt, R. Dziewior, and T. W. Hansch, *Z. Phys. B: Condens. Matter* **98**, 371 (1995); *Phys. Rev. B* **50**, 6296 (1994).
- ¹⁷M. Beau, H. Günther, G. zu Putlitz, and B. Tabbert, *Z. Phys. B: Condens. Matter* **101**, 253 (1996).
- ¹⁸S. Goyal, D. L. Schutt, and G. Scoles, *Phys. Rev. Lett.* **69**, 933 (1992).
- ¹⁹K. K. Lehmann and G. Scoles, *Science* **279**, 2065 (1998).
- ²⁰F. Stienkemeier, J. Higgins, W. E. Ernst, and G. Scoles, *Phys. Rev. Lett.* **74**, 3592 (1995).
- ²¹J. Higgins, W. E. Ernst, C. Callegari, J. Reho, K. K. Lehmann, G. Scoles, and M. Gutowski, *Science* **273**, 629 (1996).
- ²²J. P. Toennies, A. F. Vilesov, and K. B. Whaley, *Phys. Today* **54**, 31 (2001).
- ²³K. Nauta and R. E. Miller, *Science* **283**, 1895 (1999); **287**, 293 (2000).
- ²⁴D. M. Ceperley, *Rev. Mod. Phys.* **67**, 279 (1995).
- ²⁵R. P. Feynman, *Phys. Rev.* **90**, 1116 (1953); **91**, 1261 (1953).
- ²⁶P. Sindzingre, M. L. Klein, and D. M. Ceperley, *Phys. Rev. Lett.* **63**, 1601 (1989); M. V. Rama Krishna and K. B. Whaley, *ibid.* **64**, 1126 (1990).
- ²⁷M. Hartmann, R. E. Miller, J. P. Toennies, and A. F. Vilesov, *Phys. Rev. Lett.* **75**, 1566 (1995).
- ²⁸S. Grebnov, J. P. Toennies, and A. Vilesov, *Science* **279**, 2083 (1998).
- ²⁹V. S. Bibichenko and Yu. Kagan, *Phys. Rev. Lett.* **83**, 3458 (1999).
- ³⁰C. Callegari, A. Conjusteau, I. Reinhard, K. K. Lehmann, G. Scoles, and F. Dalfovo, *Phys. Rev. Lett.* **83**, 5058 (1999); **84**, 1848 (2000) (erratum).
- ³¹Y. Kwon, P. Huang, M. V. Patel, D. Blume, and K. B. Whaley, *J. Chem. Phys.* **113**, 6469 (2000).
- ³²See, for example, D. T. Anderson, R. J. Hinde, S. Tam, and M. E. Fajardo, *J. Chem. Phys.* **116**, 594 (2002).
- ³³N. Schwentner, E. E. Koch, and J. Jortner, *Electronic Excitations in Condensed Rare Gases*, Springer Tracts in Modern Physics (Springer-Verlag, Berlin, 1985), Vol. 107.
- ³⁴J. Jortner, N. R. Kestner, S. A. Rice, and M. H. Cohn, *J. Chem. Phys.* **43**, 2614 (1965).
- ³⁵M. Rosenblit and J. Jortner, *J. Phys. Chem. A* **101**, 751 (1997), and references therein.
- ³⁶A. P. Hickman and N. F. Lane, *Phys. Rev. Lett.* **26**, 1216 (1971).
- ³⁷A. P. Hickman, W. Steets, and N. F. Lane, *Phys. Rev. B* **12**, 3705 (1975).
- ³⁸J. C. Hill, O. Heybey, and G. K. Walters, *Phys. Rev. Lett.* **26**, 1213 (1971).
- ³⁹W. S. Dennis, E. Durbin, Jr., W. A. Fitzsimmons, O. Heybey, and G. K. Walters, *Phys. Rev. Lett.* **23**, 1083 (1969).
- ⁴⁰V. B. Eltsov, S. N. Dzhosyuk, A. Ya. Parshin, and Ia. A. Todoshchenko, *J. Low Temp. Phys.* **110**, 219 (1998).
- ⁴¹S. G. Kafanov, A. Ya Parshin, and Ia. A. Todoshchenko, *J. Exp. Theor. Phys.* **91**, 991 (2000).
- ⁴²A. Ya Parshin, Ia. A. Todoshchenko, and S. G. Kafanov, *Physica B* **284**, 91 (2001).
- ⁴³T. Kinoshita, K. Fukuda, and T. Yabuzaki, *Phys. Rev. B* **54**, 6600 (1996).
- ⁴⁴S. Kanorsky, A. Weis, M. Arndt, R. Dziewior, and T. W. Hansch, *Z. Phys. B: Condens. Matter* **98**, 371 (1995).
- ⁴⁵M. Beau, H. Günther, G. zu Putlitz, and B. Tabbert, *Z. Phys. B: Condens. Matter* **101**, 253 (1996).
- ⁴⁶See, for example, R. Zadoyan, J. Almy, and V. A. Apkarian, *J. Chem. Soc., Faraday Trans.* **108**, 255 (1997).
- ⁴⁷J. Eloranta and V. A. Apkarian (unpublished).
- ⁴⁸As explained in Ref. 7, the temperature-dependent triplet-triplet annihilation rate of $\text{He}_2^*(^3a)$ controlled by diffusion in LHe is used as a microscopic local thermometer, calibrated against independent measurements by J. W. Keto, F. L. Soley, M. Stockton, and W. A. Fitzsimmons, *Phys. Rev. A* **10**, 872 (1974).
- ⁴⁹For a compendium of properties of liquid helium under saturated vapor pressure, see R. J. Donnelly and C. F. Barenghi, *J. Phys. Chem. Ref. Data* **27**, 1217 (1998).
- ⁵⁰J. W. Keto, F. J. Soley, M. Stockton, and W. A. Fitzsimmons, *Phys. Rev. A* **10**, 887 (1974).
- ⁵¹G. Herzberg, *Spectra of Diatomic Molecules* (Van Nostrand Reinhold, New York, 1950).
- ⁵²For a review of classical bubble dynamics, see M. S. Plesset and A. Prosperetti, *Annu. Rev. Fluid Mech.* **9**, 145 (1977).
- ⁵³J. W. Strutt, *Philos. Mag.* **34**, 94 (1917).
- ⁵⁴W. B. Fowler and D. L. Dexter, *Phys. Rev.* **176**, 337 (1968).
- ⁵⁵H. Lamb, *Hydrodynamics*, 6th ed. (Cambridge University Press, Cambridge, 1995).
- ⁵⁶Possible distortions from spherical symmetry of the related electron bubble were considered by E. P. Gross and H. Tung-Li, *Phys. Rev.* **170**, 190 (1968).
- ⁵⁷For more recent reviews, see W. G. Flynn, in *Physical Acoustics: Principles and Methods*, edited by W. P. Mason (Academic, New York, 1964); E. A. Neppiras, *Phys. Rev.* **61**, 159 (1980).
- ⁵⁸T. Ellis and P. V. E. McClintock, *Philos. Trans. R. Soc. London, Ser. A* **315**, 259 (1985).
- ⁵⁹L. D. Landau and E. M. Lifshitz, *Fluid Mechanics*, 2nd ed. (Pergamon, Oxford, 1987).
- ⁶⁰The stages associated with shocks, followed by bubble dynamics are well analyzed in the context of underwater explosions, which was well studied during the second World War; see, for example, R. H. Cole, *Underwater Explosions* (Princeton University Press, Princeton, NJ, 1948), and for more recent reviews see Ref. 57.
- ⁶¹Reference 59, Sec. 74.
- ⁶² $N_r = 2p_0^2(\mu kT)^{1/2} e^{-\Delta/T} / (2\pi)^{3/2} \hbar^3$, where $\mu = 0.16m_{\text{He}}$ is the effective proton mass, $\Delta/k = 8.68$ K is the proton gap, and $p_0/\hbar = 1.91 \text{ \AA}^{-1}$ is the proton momentum at the gap (see Ref. 2).
- ⁶³L. D. Landau and I. M. Khalatnikov, *JETP* **19**, 637, 709 (1949).
- ⁶⁴See, for example, the related problem of proton creation by a translating electron bubble: T. Lenosky and V. Elser, *Phys. Rev. B* **51**, 12857 (1995).
- ⁶⁵C. Herring, OSRD Report No. 236, NDRC C4-sr 20-010, 1941, 1949.
- ⁶⁶W. G. Flynn, in *Physical Acoustics: Principles and Methods*, edited by W. P. Mason (Academic, New York, 1964), p. 57.
- ⁶⁷I. Rips, *J. Chem. Phys.* **106**, 2702 (1997).
- ⁶⁸M. Stone, *The Physics of Quantum Fields* (Springer-Verlag, New York, 1999).
- ⁶⁹C. E. Campbell, *J. Low Temp. Phys.* **93**, 907 (1993).
- ⁷⁰E. Madelung, *Z. Phys.* **40**, 322 (1927).